Available online at www.sciencedirect.com

SCIENCE DIRECT®

International Journal of Heat and Fluid Flow 25 (2004) 58–73

International Journal of
HEAT AND FLUID FLOW

www.elsevier.com/locate/ijhff

Vertically upward two-phase flow with a highly viscous liquid-phase in a nozzle and orifice plate

D.A. McNeil *, A.D. Stuart

Department of Mechanical and Chemical Engineering, School of Engineering and Physical Sciences, Heriot-Watt University, Nasmyth Building, Edinburgh EH14 4AS, UK

Received 14 April 2003; accepted 4 August 2003

Abstract

Water and glycerine were used to produce solutions with nominal liquid viscosities of 1, 100, 250 and 550 mPa s. These liquids flowed concurrently with air into a conical nozzle. Measurements of discharge momentum fluxes, inlet void fractions and pressure drops were made for subsonic and sonic discharges. Liquids with nominal liquid viscosities of 1 and 450 mPa s were used to do similar tests on a sharp edged orifice plate. The orifice had the same discharge diameter as the nozzle. The flow pattern developed in the long supply pipe was annular up flow. The nozzle data are shown to be consistent with the annular flow model provided the wall and interfacial shear stresses are included. The orifice plate is shown to behave in a similar manner to the nozzle, despite the very different flow path.

Keywords: Two-phase flow; Nozzles; High viscosity; Annular flow; Choked flow

1. Introduction

If a runaway reaction occurs during the manufacture of some products, such as styrene, some of the fluid needs to be blown down to protect the reactor from excessive pressure. Blowdown events are usually initiated by a safety relief valve opening or a bursting disc operating.

A safety relief valve is shown in Fig. 1. The inlet to the valve is a conical nozzle, with a parallel pipe upstream and downstream. These valves have a pop action so that when the set pressure is reached, the disc fully retracts to leave a nozzle as the flow element. When a compressible fluid passes through this nozzle, choking can occur at the throat. Many installations are designed for choked flow conditions. Standards, like API 520 (American Petroleum Institute, 1990), give details of how to calculate the nozzle area. These are based on the isentropic flow of an ideal gas through a nozzle. A bursting, or rupture, disc is shown in Fig. 2. These discs are placed in a holder and sandwiched between two flanges in the vent pipe. When the set pressure is reached, the disc comes away as shown, to leave an orifice plate as the flow element. The standards again size the flow area by using the choked isentropic nozzle flow equations. However, a discharge coefficient is introduced to compensate for the flow path deviating from the nozzle geometry.

In the circumstances envisaged for this study, a highly viscous two-phase flow will enter the safety relief valve or bursting disc. Current design knowledge is restricted in this application, causing some uncertainty in how blowdown systems will perform under these circumstances. This study was undertaken to improve the basis on which these designs are made.

Highly viscous single-phase flow of Newtonian and non-Newtonian fluids in orifice plates and nozzles have been shown to behave quite differently from their low viscosity counterparts (Alvi et al., 1978, McNeil et al., 1999, 2000). However, two-phase flows have received little attention. Some studies have been carried out in pipe flows (Furukawa and Fukano, 2001, Fukano and Furukawa, 1998, Mori and Nakano, 2001, Kondo et al., 1999). These studies used fluids with viscosities of up to 70 mPa s to investigate the effects of liquid viscosity on flow pattern, interfacial shear stress, frictional pressure

---

* Corresponding author. Tel.: +44-131-449-5111; fax: +44-131-451-3129.

E-mail address: d.a.mcneil@hw.ac.uk (D.A. McNeil).

0142-727X/$ - see front matter © 2003 Elsevier Inc. All rights reserved.
doi:10.1016/j.ijheatfluidflow.2003.08.003

Nomenclature

Capital letters

B	coefficient used in Eq. (A.1)
C	coefficient defined in Eq. (14)
D	diameter
E	coefficient used in Eq. (A.13)
F	force
FF	Froude number function
Fr	Froude number
G	constant used in Eq. (8)
H	constant used in Eq. (8)
L	length of contraction
R	gas constant
Re	Reynolds number
T	temperature
We	Weber number

Small letters

c	specific heat
g	gravitational constant
m	mass flux (total mass flow rate per unit flow area)
n	index used in Eq. (A.1)
p	pressure
u	velocity
w	work done on the liquid by the core
x	gas mass fraction (quality)
z	distance from upstream pressure tap

Greeks

ε	entrained liquid fraction
δ	film thickness
μ	viscosity
v	specific volume
σ	surface tension
τ	shear stress

Subscripts

c	core flow
C	characteristic value
d	downstream
G	gas-phase
Gs	gas superficial
i	interfacial
L	liquid-phase
s	single-phase
LF	liquid film
m	momentum
u	upstream
v	at constant volume
w	wall
W	water

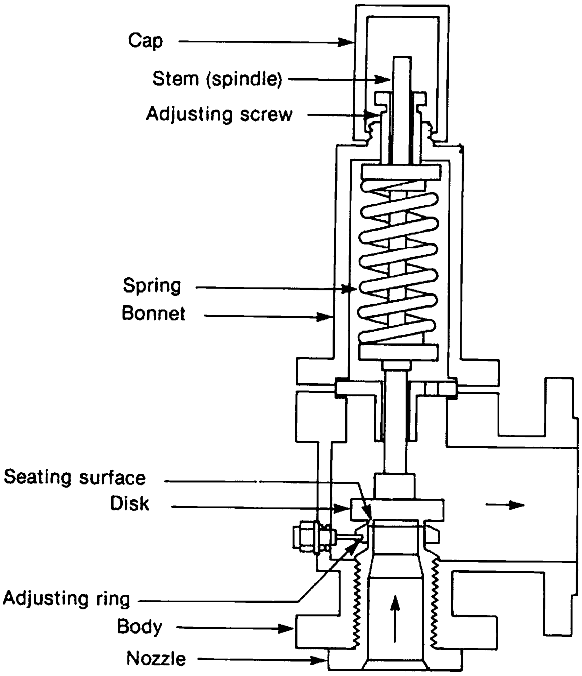

Fig. 1. Safety relief valve.

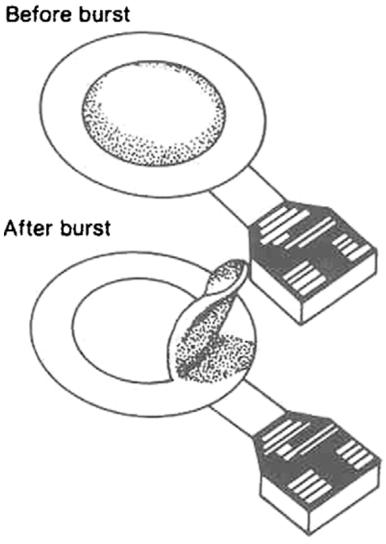

Fig. 2. Bursting disc.

drop, interfacial waves and the inception of roll waves and droplets. All of these studies have shown that increasing the liquid viscosity had a significant effect on the phenomena studied. McNeil and Stuart (2003) used liquids with a viscosity range of 1–550 mPa s with air in a pipe flow. The study showed that the higher viscosity fluids behaved differently to those with viscosities of up to the 70 mPa s. Entrained liquid fractions existed where inception criteria suggested they would not and the interfacial friction factor behaved considerably differently. Nozzle and orifice plate flows are usually downstream of a pipe length. The flow conditions at the pipe exit are therefore the inlet conditions to the nozzle or orifice plate. Studies of the effect of the altered inlet fluid distribution, resulting from elevated liquid viscosity, on the nozzle or orifice plate flow characteristics have not been previously reported.

Studies of convergent flows at elevated levels of viscosity have been undertaken, although both were carried out with downward flows. Wood and Dickson (1973) used viscosities of 37–112 mPa s in orifice plate flows. They concluded that viscosity did not have a significant effect on the flow processes and attributed this to fluid friction being relatively unimportant to these flows. To some extent Morris (1990) disagreed with this conclusion, as he was unable to include some of this data in his discharge coefficient correlation. The excluded orifice plate data had orifice to pipe diameter ratios of less than 0.418. Data taken for diameter ratios above this were included. The excluded data deviated significantly above those obtained with low viscosity fluids. Campanile and Azzopardi (2001) tested an atomising nozzle with viscosities ranging from 5000 to 50,000 mPa s. This study was mainly about liquid atomisation at the nozzle discharge, but included flow pattern observations, and void fraction and pressure drop measurements. These convergent flows were significantly affected by increasing the liquid-phase viscosity.

Most of these studies have shown that two-phase flows with a viscous liquid-phase behave substantially differently to the low viscosity equivalents. This study was initiated to investigate the differences in a vertically upward flow in a nozzle and orifice plate, and to identify a prediction method that will aid the design of venting systems for these fluids.

2. Experimental

The characteristics of flows through orifice plates or nozzles depend on the inlet flow conditions and the interaction between the geometry and the fluid. Experiments were undertaken using five different fluids in a purpose built test facility. Measurements of inlet void fraction, outlet momentum flux and pressure drop were made to investigate the effect of liquid viscosity on them.

2.1. Test fluids

The characteristics of the fluids were obtained prior to their use in the experimental programme. For tests involving water, the viscosity was taken as 1 mPa s and the density as 1000 kg/m^3. Four viscous fluids were obtained by combining glycerine with water at various concentrations. The viscosities of these solutions were obtained by analysing samples in a Carri–Med viscometer controlled by a PC. The measurements indicated that the shear stress was proportional to the strain rate and that the constant of proportionality was strongly depended on temperature, i.e., the fluids were Newtonian. The viscosity of each fluid was characterised by correlating this constant with a cubic polynomial in temperature. The densities of the test liquids were established by measuring the weight of a known volume. The glycerine–water solutions had nominal viscosities of 550, 450, 250 and 100 mPa s. The corresponding densities were 1260, 1258, 1235 and 1190 kg/m^3. The viscosity ranges present within the data for each test liquid were 430–700, 400–480, 200–260 and 70–120 mPa s. The viscosity of glycerine varies significantly with water concentration, particularly at low levels. Viscosity measurements were repeated frequently throughout the test programme.

2.2. Test facility

A schematic of the test facility is shown in Fig. 3. The facility could be operated using single-phase liquid, single-phase air or two-phase air–liquid flows. The facility had three flow loops that the liquid could pass around, the re-circulating loop, the flow meter calibration loop and the test loop. Only one loop existed for air.

The re-circulation loop had liquid from the supply tanks pass through the heat exchanger, the pump, control valve A and back to the supply tanks. This flow loop was always used when liquid was flowing. This was necessary to balance the liquid flow through the calibration or test loops with that through the progressive cavity pump. The heat exchanger was cooled using tap water and was used to control the liquid temperature by removing the internal heating resulting from pipe friction.

The calibration and test loops both used the bank of four parallel flow nozzles shown in Fig. 3. Only one of these loops was in operation at any one time. The calibration loop was used to calibrate the flow measurement nozzles prior to their use in the test loop.

The flow calibration loop took liquid from the supply tanks and passed it through the heat exchanger, the pump, a flow nozzle and control valve B, before storing it in the calibrated tanks. A thermocouple placed downstream of valve B allowed the liquid temperature to be measured, and thus allowed the liquid viscosity to be estimated. A Rosemount 3051 differential pressure transmitter was used to measure the flow nozzle pressure drop. The volume flow rate through the flow nozzle was established from a timed collection in the calibrated tanks. After the timed collection had been made, liquid was returned to the supply tanks by opening valve D.

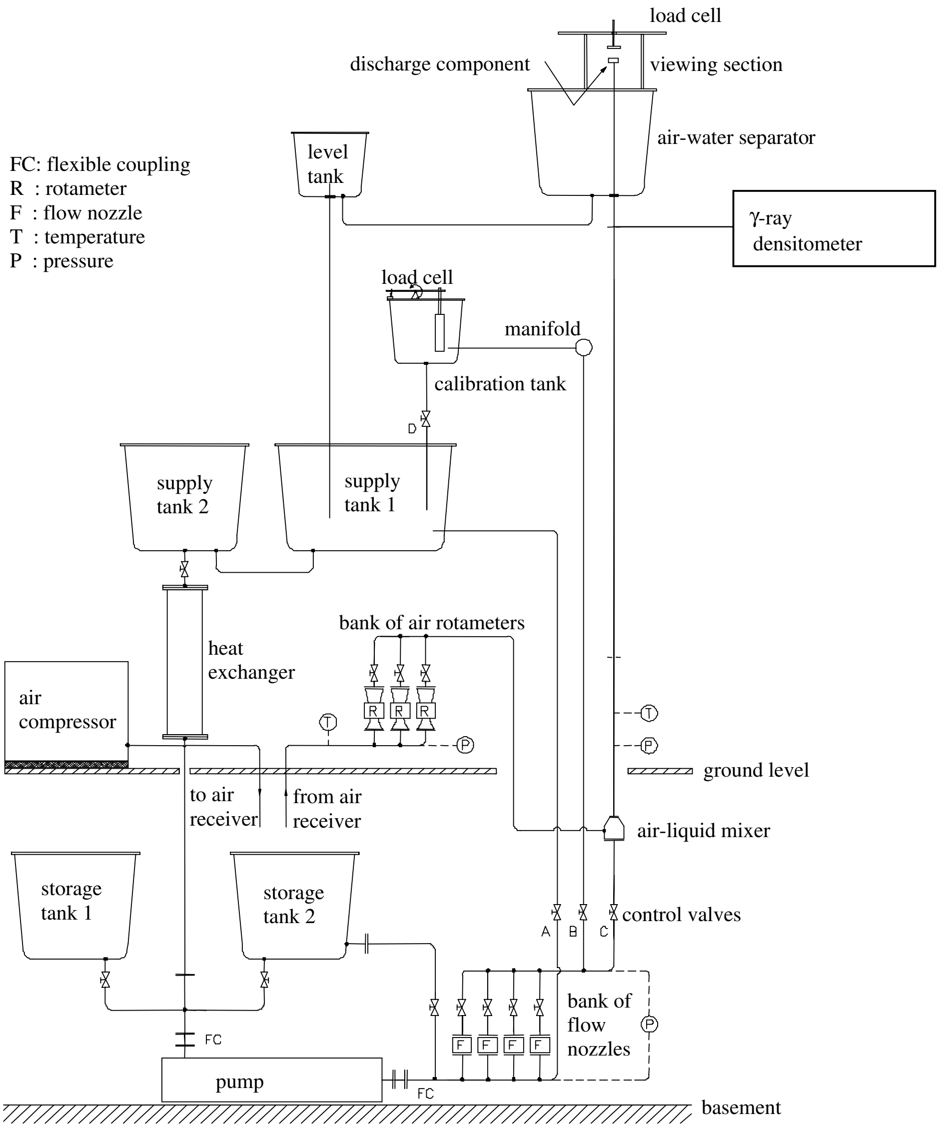

Fig. 3. Test facility layout.

For viscous liquids, the discharge coefficient depends on the throat Reynolds number (Alvi et al., 1978). The discharge coefficient was linked to the throat Reynolds number through a cubic equation.

The test loop took liquid from the supply tanks and passed it through the heat exchanger, the pump and a flow nozzle, and delivered it to control valve C (Fig. 3). A thermocouple was placed downstream of valve C to allow the test temperature to be measured. This allowed the liquid viscosity to be estimated. From valve C, the liquid moved through the air–liquid mixer, the settling length and the γ-ray densitometer, before being delivered to the discharge component. The γ-ray densitometer was located 0.905 m upstream of the discharge component and was used to determine the void fraction during the two-phase tests. The void fraction measured was the average for the flow area. The discharge component was either the nozzle or the orifice plate shown in Fig. 4. Liquid from the discharge component discharged into a glass observation chamber that was vented to the atmosphere. The discharging liquid impinged on a flat plate target set at 90° to the flow. The target was 100 mm in diameter and was placed 90 mm above the liquid discharge point. During the two-phase tests, the force on the target was measured using two load cells mounted in parallel. This allowed the momentum flow rate of the discharging mixture to be determined. Liquid flowed from the target into the air–liquid separator, where it drained into the separator liquid level control tank and onto a series of four plates angled at 30° to the horizontal. It thereafter returned to the supply tanks. The angled plates provided a surface area of 6 m^2. They were

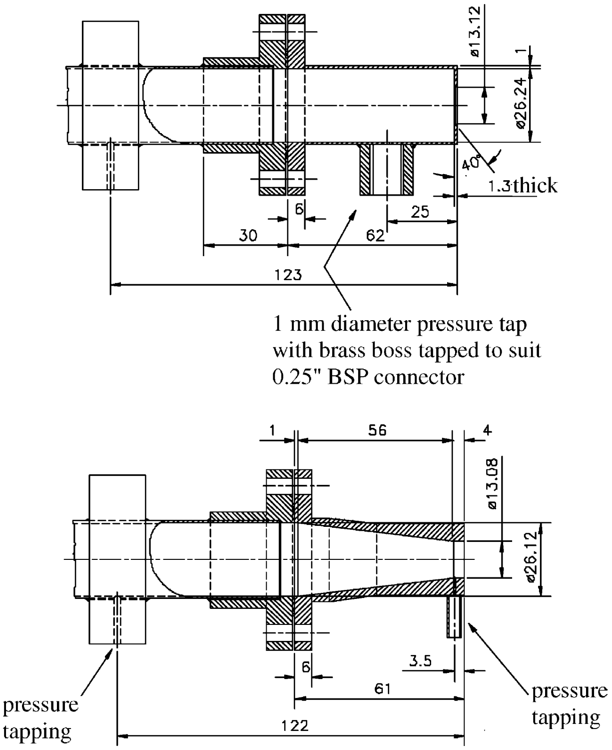

Fig. 4. Discharge fittings.

used to aid the removal of small bubbles entrained in the liquid-phase.

The air stream flowed from an air receiver that was charged to a pressure of 7.5 bar by a dedicated compressor. Filtered air from the receiver was passed to one of the three magnetically coupled rotameters. The pressure and temperature of the air entering the rotameters were measured on a Bourdon gauge and a thermocouple respectively. Air from the rotameters passed through the air–liquid mixer and into the settling length, before discharging onto the load cell target. It thereafter entered the air–liquid separator and was discharged to the atmosphere.

Two-phase operation was achieved by operating the liquid test loop and the air loop simultaneously. The liquid flow rate was established prior to the air flow-rate. The air and liquid flows were brought together via an annulus section 15 mm long, with the air occupying the inner pipe, 22 mm in diameter, and the liquid occupying the space between the outside of the air pipe and the test pipe. A two-phase flow therefore existed from the air–liquid mixer to the air–liquid separator. Additionally, when viscous liquids were used, a fan took the air from the separator exit and passed it, via a pipe, to a discharge point outside of the building. This proved a necessary additional step because very fine liquid droplets were entrained in the discharging air stream.

The high viscosity two-phase tests were particularly difficult to complete. The discharging two-phase mixture entrained very small gas bubbles in the glycerine–water solutions. Thus, over a period of time, the liquid in the supply tanks became laden with air bubbles. After about 30 min the bubbles could be viewed near the base of the glass heat exchanger. Testing ceased when this was observed, giving this as the maximum time to set the required conditions and obtain all the readings for a particular test. The heat exchanger was connected to the pump by 2.2 m of vertical pipe, 100 mm in diameter. Air-laden liquid was therefore never unintentionally injected. The small gas bubbles took about 10 h to disengage from the liquid. Immersion heaters were added to the supply tanks so that the fluid viscosity could be reduced between tests, thus allowing the air bubbles to disengage more quickly.

2.3. Test components

The details of the nozzle and orifice plate are given in Fig. 4. The length of undisturbed pipe upstream of these components was 6.9 m, giving a length to diameter ratio of 265, sufficient to give a reasonably developed flow upstream of the test component. Just inside the nozzle discharge was a pressure tap connected to a Rosemount 2088 gauge pressure transmitter. This allowed the discharge pressure to be measured so that choked flow could be detected. This and the pressure tapping 122 mm from the nozzle discharge, or 25 mm from the orifice plate, were connected to a purging/measuring system by ball valves. Also attached to this system were pressure tappings on either side of the γ-ray densitometer. These were 1.1 and 0.6 m upstream of the discharge component. The purging system was constructed from stainless steel tube 10 mm in diameter and was coupled to a Rosemount 2088 gauge pressure transmitter and to both the air and liquid supplies, allowing purging with either. Each pressure tapping was purged and read in sequence. The pressure difference across the nozzle was obtained by subtracting the downstream from the upstream reading (Fig. 4).

2.4. Miscellaneous

The γ-ray densitometer, the load cells and the pressure transmitters were read by a PC based, data acquisition system. The temperatures, the Bourdon gauge and the air rotameter readings were entered into the PC manually. 100 pressure readings and 50 load cell readings were collected and averaged for each measurement. These numbers were chosen after a study of the signals produced from a range of conditions showed them to be sufficient to determine the averages. The liquid flow nozzles were accurate to ±1% and the air rotameters to ±1.6% of reading. The pressure transmitters were of the SMART type. The operating span was set prior to a test by a HART communicator. The pressure transmitters were accurate to ±0.2% of reading. The thermocouples were K-type and were connected to a Comark microprocessor thermometer. This gave a discrimination of ±0.1 °C. The load cells were calibrated over their range of 0–4 kg by placing known weights upon them. This was repeatable to ±0.2% of reading. When the jet force exceeded the load cell range, additional know weights were placed on the target. The diameter of the supply pipe was 26 mm.

2.5. Test conditions

Two types of test were carried out on the nozzle and orifice plate, subsonic and sonic. The mass flow rates for the subsonic nozzle tests were chosen to give exit Mach numbers of about 0.5 at nominal qualities of 0.04, 0.06, 0.08, 0.1, 0.2, 0.4, 0.6 and 0.8. The Mach number estimate was based on the slip with entrained liquid fraction model of McNeil (1999), with the slip ratio and entrained liquid fraction based on the 550 mPa s fluid (Table 2). The quality was taken as the ratio of the gas mass flow rate to the total mass flow rate. Upstream mass fluxes ranging from 660 kg/m^2 s at the lowest quality to 75 kg/m^2 s at the highest quality were used. The mass flow rates for the sonic tests were arrived at by increasing the liquid and gas flows incrementally until an exit pressure above atmospheric was achieved. This was done at the same nominal qualities as the subsonic tests and gave a mass flux range of 930–150 kg/m^2 s. The nozzle was tested using mixtures with nominal liquid viscosities of 1, 100, 250 and 550 mPa s.

The mass fluxes used for the nozzle flows were also used for the viscous orifice plate flows. However, calculations based on the 'subsonic' air–water, orifice plate data indicated that choking had probably already occurred. These were therefore re-designated as the choked-flow tests. Lower mass fluxes were used to obtain actual subsonic data. The choked air–water flows therefore has a mass flux range of 90–620 kg/m^2 s while the subsonic data were obtained in the range 40–300 kg/m^2 s. The orifice plate was tested with mixtures containing liquids with nominal viscosities of 1 and 450 mPa s.

3. Flow pattern

Direct flow pattern observations were not made. The experimental conditions at the test component inlets are shown on the vertical flow map of Hewit and Roberts (1969) in Fig. 5. All of the data are shown to be in the annular flow regime. However, caution must be exercised in this assertion as Furukawa and Fukano (2001) have shown that viscosity has an effect on the flow map boundaries. The extent of the boundary shift at these viscosities is not currently quantifiable.

4. The annular flow model

Several separated flow models have been developed, e.g., Martindale and Smith (1982) and Richter (1983). A similar, but simpler, approach assumes that liquid with a specific volume v_L travels close to the wall in a liquid film of thickness δ. The gas moving in the centre of the tube has a specific volume v_G and a velocity u_c that is faster than the film velocity, u_{LF}. A fraction of the liquid, ε, is entrained in the gas to form the core flow. This liquid is assumed to travel at the gas velocity. The gas

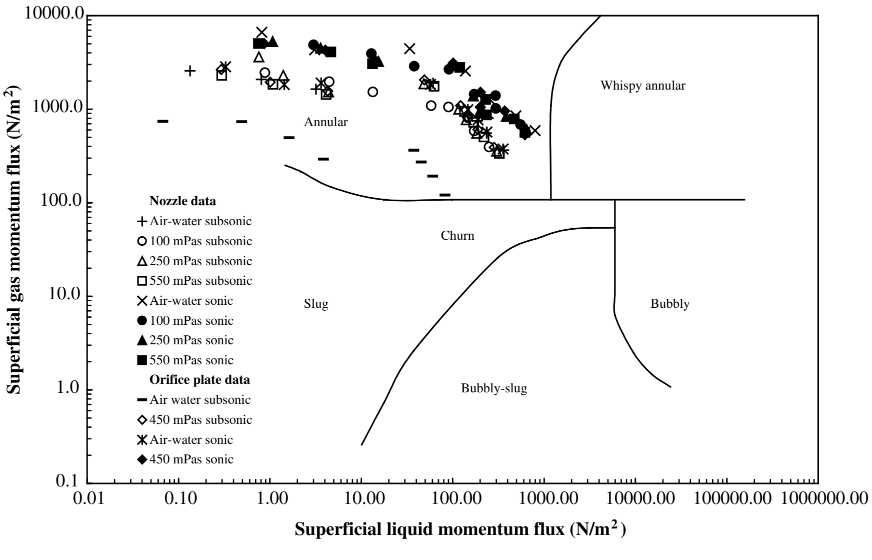

Fig. 5. Vertical flow map of Hewit and Roberts (1969).

mass fraction of the total mass flow rate is x, often referred to as the quality.

If the entrained liquid fraction is assumed constant, the momentum equation for the core flow is

$$\frac{dp}{dz} = -\frac{4\tau_i}{(D-2\delta)} - \frac{g}{v_c} - \frac{u_c}{v_c}\frac{du_c}{dz} \tag{1}$$

where p is the pressure, z is the distance from the nozzle or orifice plate inlet, D is the pipe diameter, g is the acceleration due to gravity, τ_i is the shear stress at the core liquid film interface and v_c is the specific volume of the core flow, given by

$$v_c = \frac{(xv_G + \varepsilon(1-x)v_L)}{(x+\varepsilon(1-x))} \tag{2}$$

If the core flow is adiabatic and the temperature of the entrained liquid fraction is assumed constant, the corresponding energy equation is

$$v_c\frac{dp}{dz} + \frac{x}{(x+\varepsilon(1-x))}\left(p\frac{dv_G}{dz} + c_v\frac{dT_G}{dz}\right) + u_c\frac{du_c}{dz} + g + \frac{dw}{dz} = 0 \tag{3}$$

where c_v is the specific heat at constant volume of the gas-phase, T_G is the gas temperature and dw/dz is the work done on the liquid film by the core flow, approximated by

$$\frac{dw}{dz} = \frac{4\tau_i v_c}{(D-2\delta)}\frac{u_{LF}}{u_c} \tag{4}$$

Mass continuity of the core flow requires that

$$\frac{d}{dz}\left(\frac{\pi}{4}D^2\frac{\alpha_c u_c}{v_c}\right) = 0 \tag{5}$$

The gas-phase is treated as a perfect gas of gas constant R, giving

$$v_G\frac{dp}{dz} + p\frac{dv_G}{dz} = R\frac{dT_G}{dz} \tag{6}$$

For parallel flows, the flow diameter is constant. For conical nozzle flows, the flow diameter can be expressed as

$$D = D_u + (D_d - D_u)\frac{z}{L} \tag{7}$$

where L is the length of the contraction and D_u and D_d are the upstream and downstream diameters, respectively.

The liquid film flow was modelled using an interfacial friction factor approach where the wall and interfacial shear stresses are assumed equal. For air–water flows the method of Ambrosini et al. (1991) was used. For the viscous fluids the method of McNeil and Stuart (2003) was used. The film flow method is reproduced in Appendix A.

With the liquid film flow treated as described, Eqs. (1)–(7) allow the conditions at any downstream position to be determined, once the entrained liquid fraction has been specified.

5. Conditions entering the test components

The flow entering the nozzle or orifice plate would have been approximately fully developed (Section 2.3). The upstream pressure was measured directly, Section 2.3. The upstream temperature was assumed the same as that measured downstream of valve C (Fig. 3). For analysis purposes, the other flow quantities were estimated by implementing the film model described in Appendix A. This approach requires the entrained liquid fractions to be specified at the contraction inlet. These were estimated from the correlation (Govan et al., 1998) for fully developed air–water flows, and from the extrapolating equation given by McNeil and Stuart (2003) for viscous flows. The extrapolating equations were obtained for similar viscous fluids at similar conditions and took the form

$$\sqrt{\frac{\varepsilon}{1-\varepsilon}} = H\exp(Gu_{Gs}) \tag{8}$$

where u_{Gs} is the superficial gas velocity, the gas velocity achieved when the gas flow occupies all of the pipe, and G and H are the constants listed in Table 1. As the fluid viscosity had altered slightly between the tests reported in McNeil and Stuart (2003) and those reported here, the constants used are for the closest available data.

The ranges of inlet conditions for the nozzle and the orifice plate are listed in Table 2 for subsonic flows and in Table 3 for sonic flows. The film model parameters allow the core area fraction, α_c, the fraction of the pipe area occupied by the gas and droplet flow, to be obtained from

$$\alpha_c = \left(1 - \frac{2\delta}{D}\right)^2 \tag{9}$$

with the slip ratio, k, the ratio of the average gas velocity to the average liquid velocity, following from

$$k = \frac{\varepsilon}{\alpha_c} + \frac{(1-\alpha_c)}{\alpha_c}\frac{x}{(1-x)}\frac{v_G}{v_L} \tag{10}$$

Eq. (10) results from the assumption that the gas and entrained liquid travel at the same velocity. The ranges of inlet slip ratios are included in Tables 2 and 3. Tables

Table 1
Entrained liquid fraction correlation coefficients

Viscosity (mPa s)	G (–)	H (–)
100	0.0546	0.141
250	0.0245	0.188
450	0.0292	0.127
550	0.0292	0.127

Table 2
Subsonic flow inlet conditions

Fluid viscosity (mPa s)	Discharge component (–)	Entrained liquid (–)	Film thickness (mm)	Gas velocity (m/s)	Liquid film velocity (m/s)	Shear stress (N/m^2)	Slip ratio (–)
1	Nozzle	0.00–0.55	0.10–1.0	17–41	0.78–3.3	11–42	4.2–53
1	Orifice	0.00–0.12	0.14–1.2	11–24	0.37–1.8	3.5–15	7–64
100	Nozzle	0.10–0.58	0.22–1.7	21–40	0.34–1.7	72–130	11–50
250	Nozzle	0.07–0.21	0.33–2.1	20–44	0.39–1.5	150–260	12–88
450	Orifice	0.04–0.11	0.36–2.2	22–39	0.25–1.5	150–310	14–130
550	Nozzle	0.03–0.12	0.41–2.4	20–38	0.22–1.5	160–330	13–150

Table 3
Sonic flow inlet conditions

Fluid viscosity (mPa s)	Discharge component (–)	Entrained liquid (–)	Film thickness (mm)	Gas velocity (m/s)	Liquid film velocity (m/s)	Shear stress (N/m^2)	Slip ratio (–)
1	Nozzle	0.34–0.64	0.08–0.9	18–45	1.5–4.6	28–74	3–19
1	Orifice	0.10–0.53	0.10–1.0	17–39	1.0–3.3	13–42	4.3–35
100	Nozzle	0.13–0.59	0.28–2.0	25–41	0.49–2.1	100–160	10–35
250	Nozzle	0.07–0.22	0.36–2.4	24–45	0.42–2.0	170–230	11–83
450	Orifice	0.04–0.14	0.42–2.5	22–43	0.35-1.9	190–370	11–100
550	Nozzle	0.04–0.14	0.47–2.7	24–43	0.30-1.8	200–390	13–124

2 and 3 reveal that increasing the liquid viscosity produces large increases in wall shear stress and slip ratio and significant reductions in entrained liquid fraction.

6. Void fraction measurements

The void fraction was calculated from

$$\alpha = \frac{xv_G}{(xv_G + k(1-x)v_L)} \tag{11}$$

The gas specific volume and the slip ratio were obtained at the γ-ray densitometer by applying the film model similarly to that described in Section 5, with the pressure obtained by assuming a linear variation between the pressure tappings straddling the densitometer (Section 2.3). The predicted and measured void fractions are compared in Fig. 6. The agreement is shown to be reasonable.

The increased viscosity distorts the flow map shown in Fig. 5 (Furukawa and Fukano, 2001). This is not thought to be particularly limiting to the comparisons as Holt et al. (1999) reported that the annular flow model

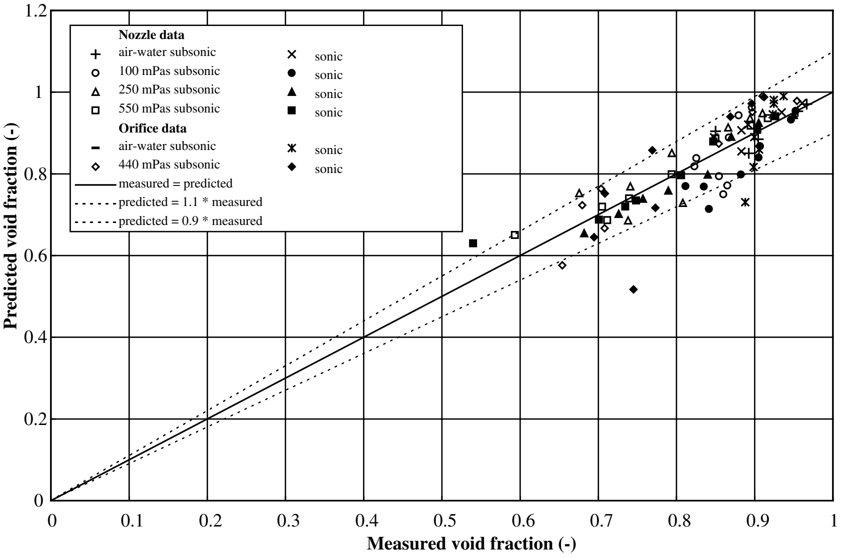

Fig. 6. Variation of predicted void fraction with measured void fraction.

works reasonably well in the annular and churn flow regimes.

7. Critical flow data

Critical flow data were obtained for the nozzle and probably the orifice plate. The nozzle data were choked because the exit pressure was 10–68 kN/m^2 above atmospheric. The orifice plate data are choked by reference to the nozzle data and the various models employed in the analysis. Several methods of determining the critical flow conditions are available. However, only 3 were used, the homogeneous flow method, a slip method and the annular flow model described in Section 4. The homogeneous flow model was selected because it is widely used. The slip method reported by McNeil (1999) was selected because it allows the supply pipe exit conditions to become the nozzle and the orifice plate inlet conditions. The values used are listed in Table 3.

The homogeneous flow model has the liquid and gas-phases travelling at the same velocity. It was implemented by including the pressure gradient due to acceleration. The frictional and gravitational pressure gradients were neglected. The liquid temperature was assumed constant and the gas was treated as perfect. This allowed the gas-phase to flow isentropically.

The slip model is constructed using the same basic flow model as that described in Section 4, i.e., it is a slip with entrained liquid model. However, like the homogeneous model, only the effects of acceleration are included. Bulk flow equations are written for momentum and energy. The liquid is assumed to flow isothermally and the gas isentropically.

Gravitational pressure drops are not important in nozzle flows. A comparison between homogeneous flow and slip flow therefore gives the effects of some of the liquid travelling at a different velocity to the gas. A comparison between the slip and annular flow models shows the effect of including wall friction.

The homogeneous and slip models depend on area reduction only. They were therefore integrated from the supply pipe area to the minimum flow area. The annular flow model was implemented differently for the nozzle and orifice plate, although, in both cases, the equations were integrating subject to the choking condition, $dz/dp = 0$, at the flow exit.

7.1. Critical nozzle flow data

For the nozzle, critical flow data were obtained when air flowed with water, the 100, 250 and 550 mPa s liquids. A comparison between the measured critical mass fluxes and the critical homogeneous flow mass fluxes, both based on the upstream flow area, is shown in Fig. 7. At the lower mass fluxes, fluxes less than 250 kg/m^2 s, which corresponds to qualities greater than 40%, the agreement is good. However, at the higher mass fluxes, agreement is poor, achieving only 70% of the measured value at the lowest quality, which corresponds to the highest mass flux.

A comparison between the measured critical mass fluxes and the critical slip flow mass fluxes is shown in Fig. 8. For flows involving water and the liquid with a viscosity of 100 mPa s, the model predicts the critical mass fluxes reasonably well across the full quality range. However, as the viscosity increases further, the agreement becomes poor.

The annular flow model described in Section 4 is flow path dependent. The equations were therefore integrated in three parts (Fig. 4). Part 1, from the upstream pressure measurement point to the beginning of the

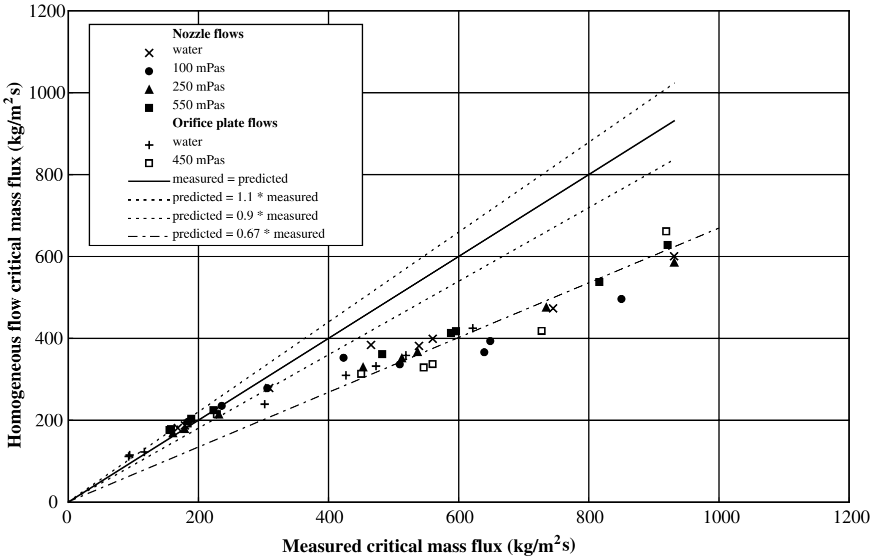

Fig. 7. Variation of homogeneous flow with measured critical mass flux.

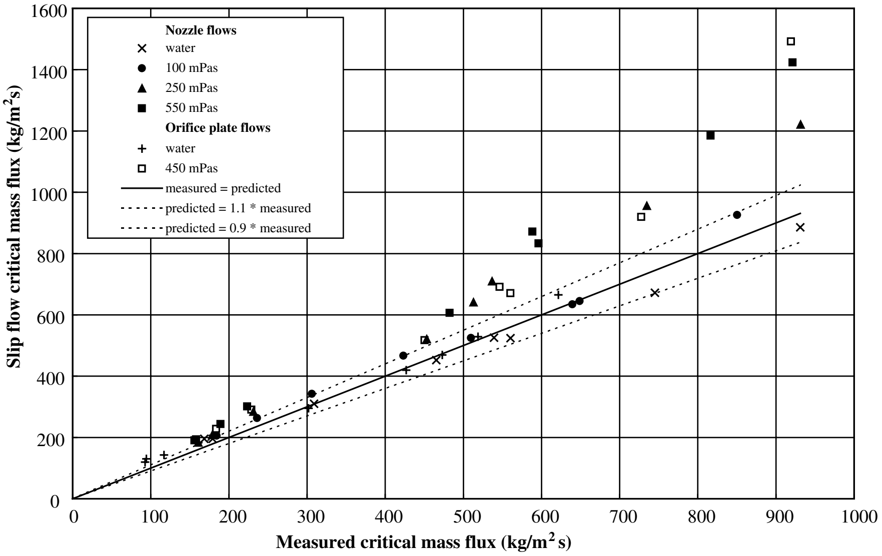

Fig. 8. Variation of slip flow with measured critical mass flux.

contraction, and part 3, from the end of the contraction to the discharge point, were treated as constant area flows. Part 2, from the start to the end of the contraction, was treated as a conical flow. A comparison between the measured critical mass fluxes and the critical annular flow mass fluxes is shown in Fig. 9. This model is shown to predict all of the data reasonably well.

The homogeneous model is an isentropic flow model. Fig. 7 indicates that at high qualities all flows can be treated as homogeneous, even though they most definitely are not (Tables 2 and 3). The slip flow model is also an isentropic flow model. A comparison between Figs. 7 and 8 shows that, for the same upstream conditions, denoted by the same measured mass flux, the mass flow rate predicted by the slip model is significantly larger than that predicted by the homogeneous flow model, and that the difference increases with increasing liquid viscosity. Increasing the viscosity increases the slip ratio and decreases the entrained liquid fraction, Table 3. This causes the increase in the predictions. However, the very large mass fluxes predicted to occur at the higher viscosities are not realised. Only the annular flow model predicts the measured critical mass fluxes for the 250 and 550 mPa s fluids. This model includes the low entrained liquid fractions and large slip ratios used in the slip model. The major difference between the slip model and the annular flow model is the inclusion of the wall and interfacial shear stresses. These are significantly larger for the two most viscous fluids (Table 3). The large mass fluxes predicted by the slip

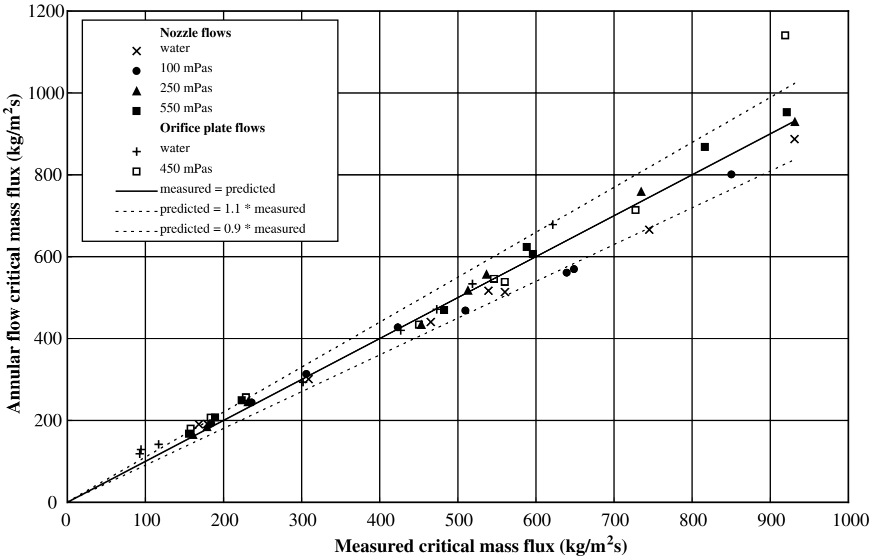

Fig. 9. Variation of annular flow with measured critical mass flux.

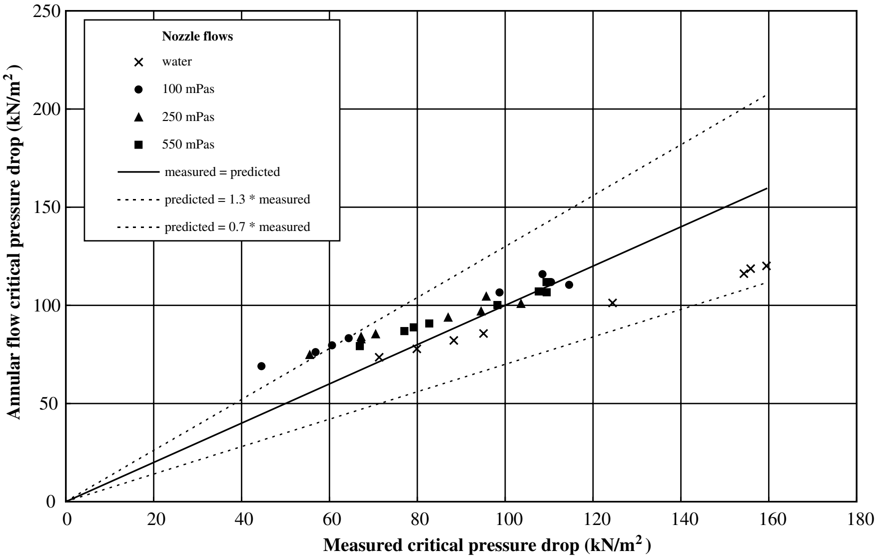

Fig. 10. Variation of annular flow with measured critical pressure drop.

model are not achieved because of the effects of wall friction. A comparison between Figs. 8 and 9 indicates that the slip flow approach is valid provided the component of pressure drop due to wall friction is negligible in comparison to that due to acceleration. In this case, this occurs when the liquid viscosity is less than 100 mPa s. Fig. 9 shows that highly viscous fluids, involving liquids with viscosities above 250 mPa s, requires the full equations to be solved.

A substantial number of data have mass fluxes that are substantially different from those predicted by the slip and homogeneous models. Comparing the corresponding predicted and measured pressure drops would therefore have little meaning. Hence, predicted and measured critical pressure drops are compared to the annular flow model only. This is done in Fig. 10. The comparison shows reasonable agreement, although a systematic error is evident across the quality range. The error appears to be independent of the liquid viscosity.

7.2. Critical orifice plate flow data

For the orifice plate, critical flow data were obtained when air flowed with water and the 450 mPa s liquid. Single-phase, orifice plate flows have a flow area that is considerably smaller than the orifice plate area. In two-phase flows this contraction only occurs at very low and very high qualities (Shannak et al., 1999). For the range of qualities obtained here, the minimum flow area can be taken as the orifice plate area. A comparison between the measured critical mass fluxes and the critical homogeneous flow mass fluxes is shown in Fig. 7. The pattern obtained for the nozzle is repeated. A comparison between the measured critical mass fluxes and the critical slip flow mass fluxes is shown in Fig. 8. Again the pattern obtained for the nozzle is repeated. The annular flow model flow path was treated as a conical flow from the pressure measurement point to the orifice plate aperture (Fig. 4). A comparison between the measured critical mass fluxes and the critical annular flow mass fluxes is shown in Fig. 9. Again this model is shown to predict all of the data reasonably well. The conclusions for the orifice plate are therefore the same as those for the nozzle. Critical pressure drop comparisons for the orifice plate cannot be made because the downstream pressure was not measured (Fig. 4).

8. Pressure drop measurements

Pressure drop measurements were made with subsonic discharges for the nozzle and orifice plate. During the nozzle tests, the downstream pressure tapping (Fig. 4), never gave a reading measurably above atmospheric. The upstream gauge pressure for the orifice plate is the pressure drop. The homogeneous flow model predicted most of the subsonic nozzle and orifice plate data to be choked, and was therefore excluded from the comparisons.

8.1. Nozzle data

The slip model pressure drops for the nozzle are compared with the measured subsonic values in Fig. 11. Also included in the figure are the sonic data that the model considered not to be choked, Fig. 8. Only the subsonic air–water data compare well with the slip model. All other data are substantially under-predicted. The annular flow model is compared to the subsonic values in Fig. 12. The comparison is reasonable. This

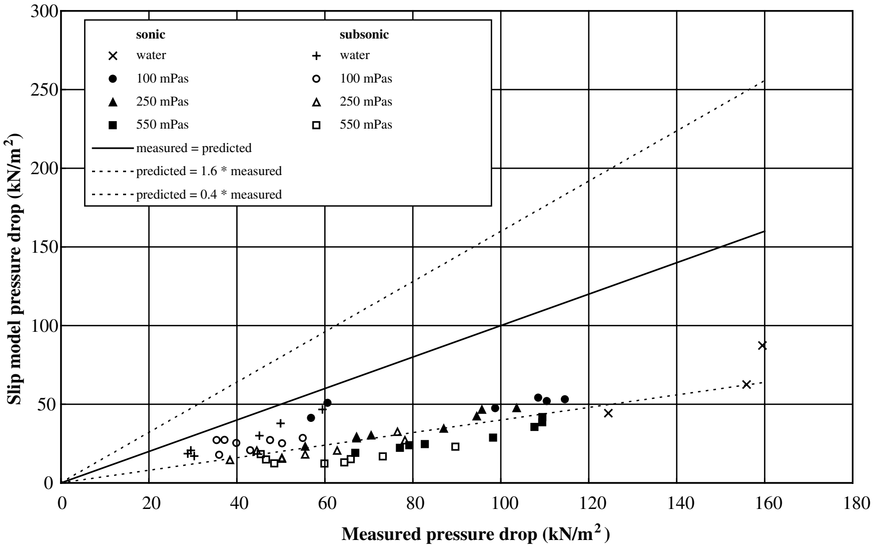

Fig. 11. Variation of the slip model pressures drop with measured values.

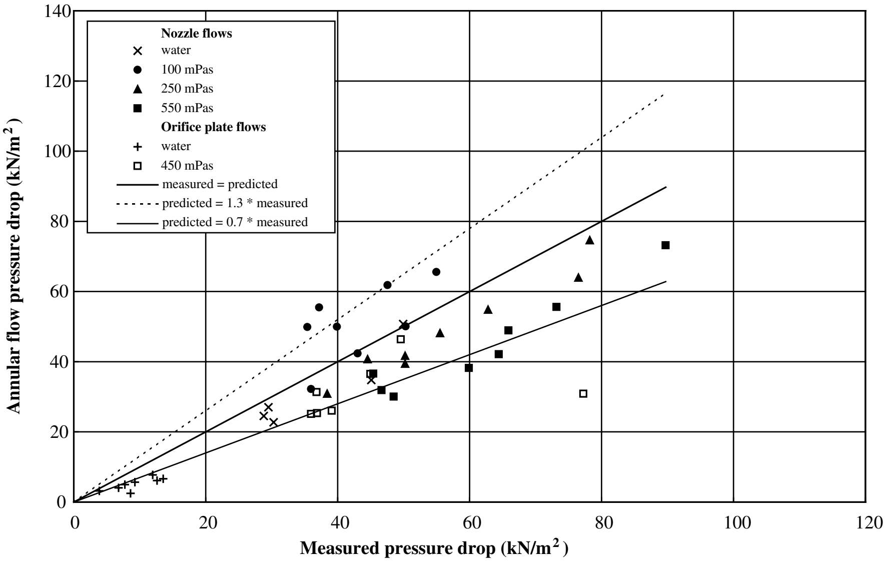

Fig. 12. Variation of annular flow with measured pressure drop.

time, however, a systematic error across the quality range is not evident.

8.2. Orifice plate data

For the orifice plate, a comparison between the annular flow pressure drops and the subsonic measurements is included in Fig. 12. Again the comparison is reasonable.

9. Jet force measurements

For the assumptions made in Section 4, the force exerted by the jet discharging from the test components onto the target can be determined from

$$F = C_{\mathrm{m}}\frac{\pi}{4}D^2 m^2 v \tag{12}$$

where m is the mass flux, the total mass flow rate per unit flow area, v is the specific volume of the two-phase mixture, given by

$$v = \frac{(xv_{\mathrm{G}} + k(1-x)v_{\mathrm{L}})}{(x + k(1-x))} \tag{13}$$

and c_{m} is the momentum correction factor that corrects for the assumed velocity distribution of the phases (see e.g., McNeil, 1998), and is given by

$$C_{\mathrm{m}} = (x + k(1-x))\left(x + (1-x)\left(\varepsilon + \frac{(1-\varepsilon)^2}{(k-\varepsilon)}\right)\right) \tag{14}$$

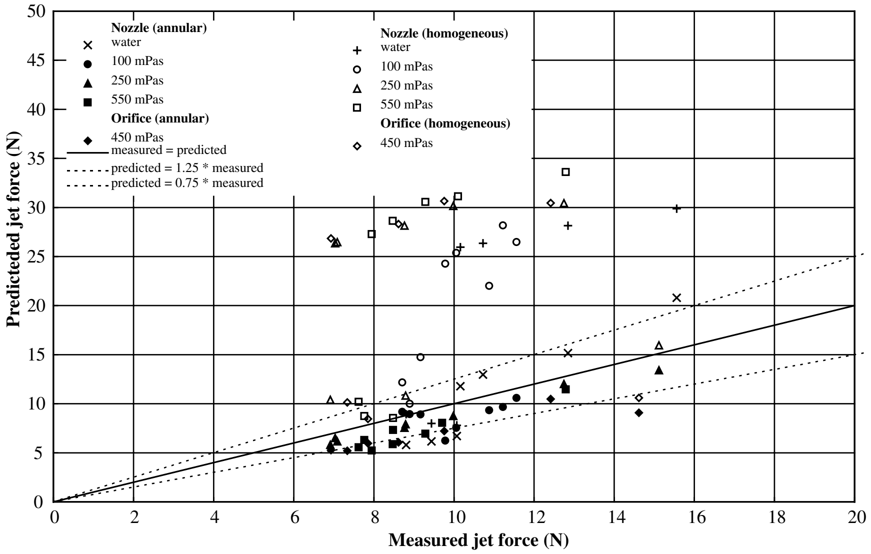

Fig. 13. Variation of predicted with measured jet force.

For a homogeneous flow, the momentum correction factor and the slip ratio are unity.

Eqs. (12)–(14) need to be evaluated at the discharge conditions. These were found by integrating the various flow models from upstream to atmospheric pressure, ignoring the predicted flow area. Jet force measurements were only obtained for subsonic discharges, since sonic discharges have a free expansion from the sonic pressure to atmospheric pressure, making the measurement method inapplicable.

9.1. Nozzle data

A comparison of the homogeneous and annular flow jet forces with the measured values for the nozzle is shown in Fig. 13. The homogeneous jet forces are shown to be significantly larger than the measured values while the annular flow values compare reasonably well. This confirms the level of entrained liquid fractions used in the comparisons, since increasing these would move the annular flow predictions upwards, towards the homogeneous values. The slip flow values are not shown since they were similar to the annular flow values, as would be expected for the same entrained liquid fractions.

9.2. Orifice plate data

Jet force measurements were not made during the orifice plate, air–water tests. The variations of the homogeneous and annular flow jet forces with the measured ones obtained with the 450 mPa s fluid are included in Fig. 13. The nozzle pattern is repeated, again confirming the assertions about the entrained liquid fraction but also justifying the assumption of a contraction coefficient of unity. A contracted flow would produce a significantly larger jet force.

10. Discussion and conclusions

Sub-critical and critical two-phase up flow data have been obtained for a nozzle and an orifice plate over a range of liquid-phase viscosities. The air–water data are consistent with current thinking since the homogeneous model can be used for high quality flows, greater than 40%, while a slip model is required for low quality flows. At first glance this could also be said for the 100 mPa s data, as the slip critical mass flux compares reasonably well with the measured values (Fig. 7). However, significant discrepancies exist in the pressure drop comparisons (Fig. 11). The homogeneous and slip models show a growing discrepancy with the critical mass flux and pressure drop data as the liquid viscosity increases. Figs. 7, 8 and 11 show that these models are inadequate when the liquid viscosity becomes large. At elevated viscosities, only the annular flow model compares well. This model compares well with the void fractions measured in the upstream pipe (Fig. 6), with the jet forces measured at the nozzle and orifice plate discharges (Fig. 13), with the subsonic pressure drops (Fig. 12), with the critical mass fluxes, Fig. 9 and with the critical pressure drops, Fig. 10. However, a systematic error is evident in the latter, indication that some model deficiency exists. This error is independent of viscosity and therefore not a result of it. The discrepancy cannot be explained by independently altering the interfacial friction factor or the entrained liquid fraction, but it can be explained by altering both simultaneously. The annular flow model is successful because the usual fundamental assumptions about the flow are invalid at these higher liquid viscosities. The entrained liquid fraction is much lower and the wall shear stress is much higher (Tables 2 and 3).

The success of the annular flow model may not be too surprising for the conical nozzle, where the flow path is controlled by the nozzle geometry. However, it is surprising that the same approach is sufficient for the orifice plate, since this flow is not so conveniently controlled by its geometry. Never the less, the patterns obtained for the orifice are the same as those obtained for the nozzle for critical mass flux (Fig. 9), pressure drop, Fig. 12 and discharge momentum, Fig. 13. The latter giving a strong indication that the contraction coefficient for the orifice plate should be taken as unity.

The conclusion from this study is that a substantial increase in liquid viscosity has a significant effect on nozzle and orifice plate flows. This is in contrast to the findings of Wood and Dickson (1973) and Morris (1990). Morris analysed the Wood and Dickson (1973) data by comparing the measured critical mass flux with the predictions of a critical flow model by McNeil and Morris (1988). This model is compared with the nozzle data from this study in Fig. 14. The agreement is very good. This model is essentially an isentropic model that contains slip ratios and entrained liquid fractions typical of low viscosity fluids, but atypical of those present in these data (Table 3). The critical mass fluxes predicted by this model are therefore in reasonable agreement with the high viscosity data because of compensating errors. The decrease in the acceleration pressure drop, brought about by the reduced entrained liquid fraction, is compensated for by the increased frictional pressure drops produced by the increased shear stress. Wood and Dickson (1973) only had overall measurements of pressure drop to work with, and were therefore misled into believing that shear stress was unimportant in these flows. Morris (1990) reported that data obtained with lower diameter ratios by Wood and Dickson (1973) behaved differently to those obtained at higher diameter ratios. This is consistent with the conclusions of this study. The smaller flow area in the orifice plate would have reduced the critical mass flow rates. The resulting low gas velocities would have produced very low entrained liquid fractions upstream of the orifice plate. Under these circumstances, the decease in acceleration pressure drop, caused by the reduced entrained liquid fraction, could have exceeded the increase in frictional pressure drop resulting from the increased shear stress. This could have caused the data to require the larger discharge coefficients reported by Morris (1990).

The study was undertaken to aid the design of vent systems for highly viscous two-phase flows. What is clear is that viscosity has a very definite effect. What is not so clear is what should be done.

The first question to pose is does the experiments reported here allow the processes in a safety relief valve or bursting disc to be reproduced? The pressure drop between the reactor and the valve is limited by the various national standards. This means that most valves are located close to the reactor. The flow path into the valve therefore depends on how the fluid exits the vessel. This is an unknown at this time, but the flow may not be annular. If the valve is located some distance from the reactor, an annular flow may result, irrespective of how the fluid exits the reactor. However, as was observed at the fluid discharge and described in Section 2.2, agitation of the two-phase mixture causes small gas bubbles to be entrained in the liquid-phase. The effect that these may have on the fluid flow is unknown. Further work is therefore required on how fluid exits the vessel, on flow parameters for other flow patterns and on the effect of

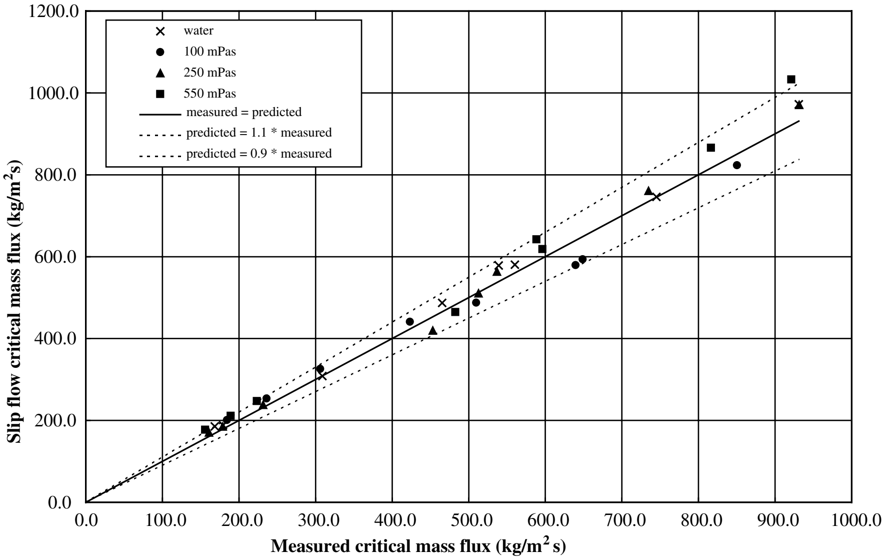

Fig. 14. Variation of the McNeil and Morris with measured critical mass flux.

entrained gas bubbles on pipe friction and the entraining processes. This latter issue is compounded by the fact that the annular flow model requires an entrained liquid fraction to be calculated, something that currently cannot be done for a highly viscous liquid (McNeil and Stuart, 2003).

If the results obtained are representative of flow in safety valves and rupture discs, the consequences for a blowdown system need to be clarified. The annular flow model was used to simulate flows for the same range of liquid viscosities and qualities. However, the upstream pressure and temperature were kept constant to simulate the flow rates that would be obtained from a reactor. The critical mass fluxes passed by the nozzle and the orifice plate were up to 25% larger at the largest liquid viscosity. This seemed like a surprising result, since increasing the viscosity increases the wall shear stress (Table 3), which should lead to a reduction in mass flow. However, the flow capacity of a two-phase contraction increases as the slip ratio increases and the entrained liquid fraction decreases. These also occur as the viscosity increases (Table 3). What these simulations showed was that the flow capacity increase associated with the increase in slip ratio and the decrease in the entrained liquid, exceeded the flow capacity reduction associated with the increase in shear stress. This may not be the case at higher liquid viscosities. Some groups, like DIERS, the Design Institute for Emergency Relief Systems, currently recommend that vent sizes should be obtained by applying homogeneous equilibrium theory. This will produce an even more conservative estimate of the flow rate than the annular flow model used in the simulations. If vents were designed by this method for the fluids tested in this study, the venting systems would be over sized and therefore more expensive than they need be. Also, the processing equipment downstream of the vent may be undersized. Further study into the effects of a highly viscous liquid-phase is therefore recommended.

Acknowledgements

The authors gratefully acknowledges the financial support given to this work by the European Commission (DGXII-Science, Research and Development) through the INOVVATOR project (Environment and Climate programme).

Appendix A. Film flow model

The thickness of the liquid film was evaluated using the method of Ambrosini et al. (1991). This method related a non-dimensional film thickness, δ_L^+, to the film Reynolds number, Re_{LF}, through

$$\delta_L^+ = BRe_{LF}^n = \frac{\delta}{\mu_L}\sqrt{\frac{\tau_C}{v_L}} \tag{A.1}$$

where μ_L is the liquid viscosity. The liquid film Reynolds number is given by

$$Re_{LF} = \frac{(1-\varepsilon)(1-x)mD}{\mu_L} \tag{A.2}$$

where m is the total mass flow rate per unit pipe area. When the film Reynolds number is less than 1000, the flow is laminar and the coefficient B and the index n are 0.34 and 0.6 respectively. When the film Reynolds number is greater than 1000, the flow is turbulent and the coefficient B and the index n are 0.0512 and 0.875 respectively. The characteristic shear stress, τ_C, is given by

$$\tau_C = \frac{(\tau_i + 2\tau_w)}{3} \tag{A.3}$$

where τ_w is the wall shear stress. The interfacial shear stress, τ_i, is obtained through an interfacial friction factor, f_i, defined through

$$\tau_i = \frac{f_i}{2}\frac{u_c^2}{v_G} = \frac{f_i}{2}\left(\frac{xm}{\alpha}\right)^2 v_G \tag{A.4}$$

The interfacial friction factor depends on whether the liquid-phase has a high or low viscosity. In this study water has a low viscosity and all other liquids had high viscosities. The equations are solved subject to the assertion that the interfacial and wall shear stresses are the same.

A.1. Interfacial friction factor for low viscosity systems

The interfacial friction factor for low viscosity systems was obtained from the Ambrosini et al. (1991) method. This method relates the interfacial friction factor to a non-dimensional gas film thickness, δ_G^+, defined through

$$\delta_G^+ = \frac{\delta}{\mu_G}\sqrt{\frac{\tau_i}{v_G}} \tag{A.5}$$

where μ_G is the viscosity of the gas-phase. The interfacial friction factor is then

$$f_i = f_s\left(1 + 13.8\frac{We^{0.2}}{Re_G^{0.2}}\left(\delta_G^+ - 200\sqrt{\frac{v_L}{v_G}}\right)\right) \tag{A.6}$$

where We is the Weber number, defined through

$$We = \left(\frac{xm}{\alpha}\right)^2\frac{Dv_G}{\sigma} \tag{A.7}$$

Re_G is the gas Reynolds number, obtained from

$$Re_G = \frac{xmD}{\alpha\mu_G} \tag{A.8}$$

f_s is the friction factor for a smooth tube, obtained from

$$f_s = \frac{0.046}{Re_G^{0.2}} \tag{A.9}$$

and σ is the liquid surface tension.

A.2. Interfacial friction factor for high viscosity systems

The interfacial friction factors for high viscosity systems are obtained from a Froude number function, FF, defined through

$$\mathrm{FF} = \frac{1}{Fr^{1.28}}\left(\frac{v_{\mathrm{G}}}{v_{\mathrm{L}}}\right)^{0.912} \tag{A.10}$$

where the Froude number is defined by

$$Fr = \frac{u_{\mathrm{c}}}{\sqrt{g\delta}} \tag{A.11}$$

These fluids are characterised by a smooth film-rough film behaviour. The smooth film behaviour is described by

$$f_{\mathrm{i}} = 0.0983\mathrm{FF}^{0.249} \tag{A.12}$$

and the rough film behaviour by

$$f_{\mathrm{i}} = E \times \mathrm{FF} \tag{A.13}$$

where E is a constant obtained from

$$E = 0.286 + 0.00153\frac{\mu_{\mathrm{L}}}{\mu_{\mathrm{W}}} \tag{A.14}$$

and μ_{w} is the viscosity of water at 20 °C.

The data on this rough line have a liquid Reynolds number of less than 40. If the liquid Reynolds number, found by assuming that the liquid flows alone in the pipe, is less than 40, the rough coefficient is 1.12, otherwise it comes from Eq. (A.14) provided it does not exceed 1.12. The transition Froude number function follows by equating Eqs. (A.12) and (A.13). The friction factor is then found by assuming a smooth flow. If the resultant Froude number function is less than the transition value, the smooth value is appropriate, otherwise the friction factor must be re-calculated assuming a rough film.

References

Alvi, S.H., Sridharan, K., Lakshmana Rao, N.S., 1978. Loss characteristics of orifices and nozzles. J. Fluid Eng. 100, 299–307.

Ambrosini, W., Andreussi, P., Azzopardi, B.J., 1991. A physically based correlation for drop size in annular flow. Int. J. Multiphas. Flow 17, 497–507.

American Petroleum Institute (API), 1990. Sizing, selection and installation of pressure-relieving devices in refineries API Recommended Practice 520, fifth ed., July 1990.

Campanile, F., Azzopardi, B.J., 2001. Two-phase downflow and atomisation of very viscous liquids. In: Proceeding of the Fourth International Conference on Multiphase Flow, New Orleans, 27 May–1 June 2001, Paper 827.

Fukano, T., Furukawa, T., 1998. Prediction of the effects of liquid viscosity on interfacial shear stress and frictional pressure drop in vertical upward gas–liquid annular flow. Int. J. Multiphas. Flow 24, 587–603.

Furukawa, T., Fukano, T., 2001. Effects of liquid viscosity on flow patterns in vertical upward gas–liquid two-phase flow. Int. J. Multiphas. Flow 27, 1109–1126.

Govan, A.H., Hewitt, G.F., Bott, T.R., Owen, D.G., 1998. An Improved CHF Modelling Code. In: Proceeding of the Second UK National Conference on Heat Transfer, University of Strathclyde, Glasgow, Paper C175/88, pp. 33–48.

Hewit, G.F., Roberts, D.N., 1969. Studies of two-phase flow patterns in simultaneous flash and X-ray photography. AERE-M2159, Harwell.

Holt, A.J., Azzopardi, B.J., Biddulph, M.W., 1999. Calculation of two-phase pressure drop for vertical upflow in narrow passages by means of a flow pattern specific model. Trans. IChem. E Part A 77, 7–15.

Kondo, Y., Mori, K., Yagishita, T., Nakabo, A., 1999. Effect of liquid viscosity on wave behaviour in gas–liquid two-phase flow. In: Proceedings of the Fifth ASME/JSME Joint Thermal Conference, San Diego, CA, 15–19 March 1999, pp. 1–8.

Martindale, W.R., Smith, R.V., 1982. Separated two-phase flow in a nozzle. Int. J. Multiphas. Flow 8, 217–226.

McNeil, D.A., 1998. Two-phase momentum flux in pipes and its application to incompressible flow in nozzles. In: Proceedings of the Institution of Mechanical Engineers: Part CJ. Mech. Eng. Sci. 212, 631–641.

McNeil, D.A., 1999. A slip with entrained liquid fraction approach to compressible two-phase flow in nozzles. In: Proceedings of the Institution of Mechanical Engineers: Part CJ. Mech. Eng. Sci. 213, 729–740.

McNeil, D.A., Morris, S.D., 1988. A simple explicit method for estimating gas/liquid choked flow conditions in pipeline restrictions. In: Proceeding of the Second UK National Conference on Heat-Transfer, University of Strathclyde, Glasgow, Paper C143/88, pp. 1243–1256.

McNeil, D.A., Stuart, A.D., 2003. The effects of a highly viscous liquid phase on vertically upward two-phase flow in a pipe. Int. J. Multiphas. Flow 29, 1523–1549.

McNeil, D.A., Addlesee, A.J., Stuart, A.D., 1999. An experimental study of viscous flows in contractions. J. Loss Prevent. Process Ind. 12, 249–258.

McNeil, D.A., Addlesee, A.J., Stuart, A.D., 2000. Newtonian and non-Newtonian viscous flows in nozzles. In: Proceedings of the Institution of Mechanical Engineers: Part CJ. Mech. Eng. Sci. 214, 1425–1436.

Mori, K., Nakano, K., 2001. Effects of liquid viscosity on inception of disturbance waves and droplets in gas–liquid two phase flow. Exp. Heat Transfer, Fluid Mech. Thermodyn., Thessaloniki, 1829–1834.

Morris, S.D., 1990. Discharge coefficients for choked gas–liquid flow through nozzles and orifices and applications to safety devices. J. Loss Prevent. Process Ind. 3, 303–310.

Richter, H.J., 1983. Separated two-phase flow model: application to critical two-phase flow. Int. J. Multiphas. Flow 9, 511–530.

Shannak, B.B., Friedel, L., Alhusein, M., 1999. Prediction of single- and two-phase flow contraction through a sharp edged short orifice. Chem. Eng. Technol. 22, 865–870.

Wood, J.D., Dickson, A.N., 1973. Metering of oil-air mixtures with sharp edged orifices. Department of Mechanical Engineering Report, Heriot-Watt University, Riccarton, Edinburgh, UK.